

Doped two-dimensional diamond: properties and potential applications

Bruno Ipaves*

Instituto de Física, Universidade de São Paulo, CEP 05508-090 São Paulo, SP, Brazil

João F. Justo†

Escola Politécnica, Universidade de São Paulo, CEP 05508-010, São Paulo, SP, Brazil

Biplab Sanyal‡

Department of Physics and Astronomy, Uppsala University, 75120 Uppsala, Sweden

Lucy V. C. Assali§

Instituto de Física, Universidade de São Paulo, CEP 05508-090 São Paulo, SP, Brazil

(Dated: August 21, 2023)

This paper examines the structural, thermodynamic, dynamic, elastic, and electronic properties of doped 2D diamond C_4X_2 ($X = B$ or N) nanosheets in both $AA'A''$ and ABC stacking configurations, by first-principles calculations. Those systems consist of three diamond-like graphene sheets, with an undoped graphene layer between two 50% doped ones. Our results, based on the analysis of *ab-initio* molecular dynamics simulations, phonon dispersion spectra, and Born's criteria for mechanical stability, revealed that all four structures are stable. Additionally, their standard enthalpy of formation values are similar to the one of pristine 2D diamonds, recently synthesized by compressing three graphene layers together. The C_4X_2 ($X = B$ or N) systems exhibit high elastic constant values and stiffness comparable to the diamond. The C_4N_2 nanosheets present wide indirect band gaps that could be advantageous for applications similar to the ones of the hexagonal boron nitride (h-BN), such as a substrate for high-mobility 2D devices. On the other hand, the C_4B_2 systems are semiconductors with direct band gaps, in the 1.6 - 2.0 eV range, and small effective masses, which are favorable characteristics to high carrier mobility and optoelectronics applications.

I. INTRODUCTION

Graphene is the most popular two-dimensional (2D) material, being a zero-gap semimetal with a honeycomb carbon structure and sp^2 hybridization. It carries a unique combination of physical properties in nature, such as high electrical conductivity, tensile strength, and optical transparency. Additionally, it is the elementary structure for several other nanomaterials, such as fullerenes, nanotubes, graphite, and the single-layer diamond (2D diamond) [1–3]. As a result of recent developments in the synthesis and characterization of 2D materials, the 2D diamond has received great attention, with promising applications in several fields, such as batteries, quantum computing, nano-optics, and nanoelectronics [4].

The stabilization of 2D diamond often requires surface functionalization, leading to a variety of structures, which have received different labels, such as diamane, diamene, diamondol, and diamondene [4, 5]. 2D diamonds can also be built out of bilayer graphene (BLG) or few-layer graphene (FLG) through different techniques. For example, the hydrogenated (HD) and fluorinated (FD) 2D diamonds can be synthesized at ambient pressure without a substrate, in which the HD can be produced

using hot filament chemical vapor deposition (CVD) [6], while FD by combining FLG and gaseous ClF_3 [7].

The pristine 2D diamond (PD) is hard to synthesize as high pressures are required to transform sp^2 bonds from graphene layers into interlayer sp^3 ones [5]. Nevertheless, the PD has recently been synthesized without a substrate, by compressing three graphene layers [8]. Additionally, a theoretical investigation has shown that it is possible to stabilize the 2D diamond made of two graphene layers with nitrogen substitution [9]. For example, the NCCN 2D structure, composed of two carbon layers functionalized with nitrogen ones on both sides, has also been investigated, suggesting it could be used as a selective ammonia sensor [10–12].

The physical properties of 2D diamonds may vary considerably, depending on the synthesis methods, leading to structures with different configurations, functional groups, and heteroatoms [4, 5]. At room temperature, the thermal conductivity of HD is high and the heat transport arises from the acoustic phonon modes. On the other hand, under the same conditions, the thermal conductivity of FD is lower than that of HD and the heat transport is controlled by the optical phonon modes [13]. 2D diamonds also present remarkable mechanical properties, with stiffness and Young's modulus similar to the ones of graphene and bulk diamond [14]. Furthermore, unlike graphene, 2D diamonds have band gap features that depend on the stacking arrangement, the number of layers, and the functional groups present in the structures [4, 15]. Despite several recent experimental and theoretic

* ipaves@if.usp.br

† joao.justo@usp.br

‡ biplab.sanyal@physics.uu.se

§ lassali@if.usp.br

cal investigations on 2D diamonds, the origin of all these peculiar properties has been the subject of debate [4, 5].

In this paper, we present a study of the physical properties of 2D diamonds doped with substitutional N or B atoms. The reference systems consist of three graphene sheets: an undoped graphene layer between two 50% doped ones, where the C-C bonds between neighboring layers are strong covalent bonds. Here, we considered four structure configurations labeled AA'A''-C₄N₂, ABC-C₄N₂, AA'A''-C₄B₂, and ABC-C₄B₂. Their structural, thermodynamic, dynamic, elastic, and electronic properties and potential applications are explored and discussed in depth.

II. COMPUTATIONAL METHODS

This investigation was performed using first-principles calculations based on the Density Functional Theory (DFT) [16], using the plane-wave basis set and projector augmented-wave (PAW) method [17], as implemented in the Quantum ESPRESSO computational package [18, 19]. We utilized the generalized gradient approximation of Perdew–Burke–Ernzerhof (GGA-PBE) exchange–correlation functional [20] and the Dion *et al.* scheme [21] optimized by Klimeš *et al.* (optB88-vdW [22]) to properly describe the effects of the dispersive van der Waals (vdW) interactions. For an accurate description of the energy band gap values, we employed the hybrid Heyd-Scuseria-Ernzerhof (HSE) functional [23] at the relaxed structures obtained from the optB88-vdW approximation. The plane-wave energy cutoff was set to 1100 eV with a convergence threshold of 0.1 meV/atom for the total energy. We used a $16 \times 16 \times 1$ k -point mesh to describe the irreducible Brillouin zone [24], and the forces on atoms were converged down to 1 meV/Å. To obtain the phonon dispersion curves, we used the Density Functional Perturbation Theory (DFPT) [25] with an $8 \times 8 \times 1$ q -point mesh.

The primitive hexagonal cells of the 2D structures were constructed using 6 atoms. To determine the cell parameters in the xy -plane, a variable-cell optimization was carried out with the BFGS quasi-newton algorithm. In order to avoid interactions among cell images, the lattice parameter perpendicular to the sheets (z -axis) was fixed at 25 Å. This approach has been successfully applied to similar 2D systems in previous studies [10, 26, 27].

In order to determine the elastic properties of the systems, we built a rectangular cell with 12 atoms and used the strain–energy method [28, 29]. Accordingly, for isotropic structures and small deformations (ϵ) near their equilibrium configurations, the elastic energy, per unit area, was approximated as

$$E(\epsilon) - E(0) \approx \frac{1}{2} E^{(2)} \epsilon^2, \quad (1)$$

where $E(\epsilon)$ is the total energy of strained configurations, while $E(0)$ is the total energy of the respective unstrained

ones. We applied two in-plane deformations, ranging from -1.2% to 1.2%, in order to obtain the $E^{(2)}$, which allowed to obtain the elastic constants after fitting a second-order polynomial to the data. Herein, $E^{(2)} = C_{11}$ elastic constant for the zigzag axial deformation, while $E^{(2)} = 2(C_{11} + C_{12})$ for the biaxial planar deformation [28, 29].

The thermal stability was studied by computing the standard enthalpy of formation, per atom, of the structures at 0 GPa (ΔH_f^0), by using

$$\Delta H_f^0 = \frac{E_t(C_4X_2) - 4E_t(C) - 2E_t(X)}{6}, \quad (2)$$

where $E_t(C_4X_2)$ is the total energy of the 2D nanosheet, with 4 C atoms and 2 X atoms ($X = B$ or N) in the primitive cell. $E_t(C)$ and $E_t(X)$ are the total energies, per atom, of the respective C and X standard ground states, i.e., of graphite and the crystalline boron in the trigonal structure (β -boron) or the isolated N₂ molecule. This procedure to determine enthalpies and/or energies of formation has been successfully used to investigate several other systems [30–34].

Additionally, *ab-initio* molecular dynamics simulations (AIMD) were carried out using the Vienna *ab initio* simulation package (VASP) [35], where a $6 \times 6 \times 1$ hexagonal 216-atom supercell was adopted to allow possible structural reconstructions. A Nose–Hoover thermostat (NVT) ensemble was employed, from 300 to 1000 K for 5 ps, with a simulation time step of 1 fs.

III. RESULTS AND DISCUSSION

Initially, we explored the physical properties of pristine 2D diamond in AA'A'' and ABC stacking structural configurations, composed of three graphene layers in which the C atoms between layers are covalently bonded with a near sp^3 hybridization. Starting the simulations with the diamond-like configuration, they converged, after the relaxation of atomic positions, to trilayer graphene systems with vdW interactions between layers (graphite-like). This behavior has also been found in a previous theoretical investigation of 2D diamond, starting the simulations with two graphene layers [36]. These results can be understood as a consequence of the absence of an external pressure-induced and/or surface passivation to promote the sp^2 to sp^3 hybridization transformation [36]. Those pristine structures represent the reference systems used here to study and understand the effects of their functionalization.

Then, we explored the properties of C₄X₂ ($X = B$ or N) systems, which can be described as three graphene sheets in which four C atoms are bonded covalently (2D diamond-like) in each unit cell. The two external layers are 50% doped with substitutional X atoms, hence, each X atom is bonded to three C atoms. Figure 1 presents a schematic representation of the optimized and relaxed C₄X₂ ($X = B$ or N) systems, in both AA'A'' and ABC

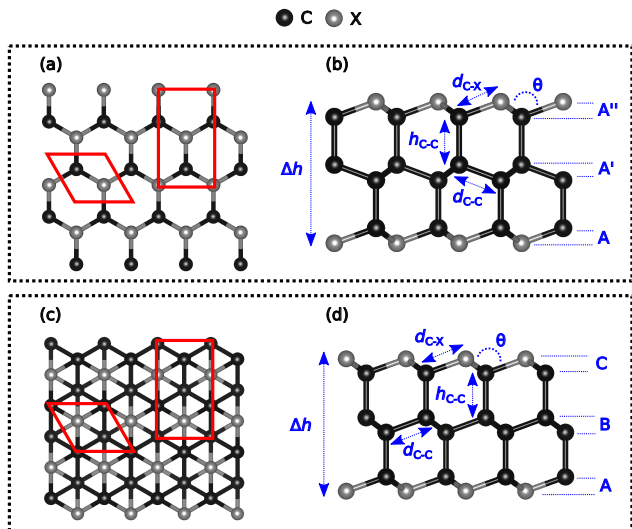


FIG. 1. Schematic illustration of the C_4X_2 ($X = B$ or N) systems. (a) Top and (b) side views of $AA'A''-C_4X_2$, (c) top and (d) side views of $ABC-C_4X_2$. The black and gray spheres represent the C and X atoms, respectively. The red lines denote the simulation unit cell limits, with the rectangle cells used to determine the elastic properties. The graphs also indicate the labels given to the intralayer (d_{C-X}) and interlayer (h_{C-X}) distances, structure thickness (Δh), and the intraplanar bond angle (θ).

TABLE I. Structural properties of C_4X_2 ($X = B$ or N): lattice parameter (a), intralayer (d) and interlayer (h) distances, thickness (Δh), and the intraplanar bond angle (θ), labeled according to figure 1. The distances are given in Å and angles in degrees. The standard enthalpies of formation (ΔH_f^0) at 0 GPa are given in meV/atom. For PD, HD, and FD, $X = C$.

System	a	d_{C-X}	d_{C-C}	h_{C-C}	Δh	θ	ΔH_f^0
$AA'A''-C_4N_2$	2.42	1.49	1.49	1.60	4.74	108.9	348
$ABC-C_4N_2$	2.44	1.50	1.50	1.57	4.66	109.0	333
$AA'A''-C_4B_2$	2.66	1.55	1.62	1.66	4.25	118.4	424
$ABC-C_4B_2$	2.67	1.55	1.63	1.65	4.18	118.5	365
PD ^a	2.43	Y ^a	1.54	1.65	—	Y ^a	300
HD ^b	2.53	1.56	—	1.56	—	—	—
FD ^b	2.56	1.55	—	1.55	—	—	—
NCCN	2.39 ^c	1.47 ^c	—	1.58 ^c	2.59 ^d	108.8 ^c	211 ^d

^a Reference [8]. The $(\bar{2}110)$ -oriented h-diamane exhibits two d_{C-X} and θ values. Y = bond lengths are 1.35 and 1.54 Å with the angles presenting sp^3 and sp^2 hybridizations.

^b Reference [15]

^c Reference [10]

^d Reference [9]

stacking configurations, as well as the respective labels given to the intraplanar bond angle (θ), intralayer (d_{C-X}) and interlayer (h_{C-X}) distances, and systems' thickness (Δh).

The optimized structural parameters of C_4X_2 ($X = B$ or N) nanosheets are shown in Table I, where the distance labels are consistent with the ones defined in figure

1. It can be observed that all the nanosystems functionalized with N atoms keep the lattice constants almost unchanged when compared to the PD ones. Additionally, for both stacking configurations of the C_4N_2 , the intraplanar bond angle (θ) values are close to the sp^3 hybridization ones (109.47°), leading to a thickness of ≈ 4.7 Å. Nevertheless, the C_4B_2 nanosheet lattice parameters are slightly greater than those of HD and FD systems, with θ close to the value of 120° , i.e., the B atoms bonded to three adjacent C atoms present a sp^2 -type hybridization and hence we observed a smaller thickness of ≈ 4.2 Å as compared to the N-functionalized structures.

We now discuss the stability of the C_4X_2 nanosheets. To study the thermal stability of those structures, we computed the standard enthalpy of formation ΔH_f^0 using equation (2). Herein, we found positive ΔH_f^0 of 424, 365, 348, and 333 meV for $AA'A''-C_4B_2$, $ABC-C_4B_2$, $AA'A''-C_4N_2$, and $ABC-C_4N_2$, respectively, displayed in Table I, indicating possible thermodynamic instability. However, the literature has reported 2D materials synthesized by endothermic processes ($\Delta H_f^0 > 0$), such as graphene, germanene, and silicene [29, 33]. Also, the ΔH_f^0 values of C_4X_2 nanosheets are similar to the 300 meV/atom of PD with three graphene layers at 0 GPa (Table I), which was recently synthesized [8], and slightly higher than NCCN that was theoretically studied to stabilize the 2D diamond without any passivation [9].

The thermodynamic stability of the systems was also investigated by AIMD simulations. The results exhibited a total energy small variation during 5 ps at 300 K, as shown in figure 2, indicating that the structural integrity of those systems is maintained at those conditions. At 1000 K, the same behavior is observed for the C_4N_2 systems, while the C_4B_2 nanosheets presented some broken bonds, suggesting some structural degradation.

Furthermore, the dynamic stability of the systems was investigated using the phonon theory, in which a system is considered stable when its vibrational spectrum contains only positive frequencies. The phonon dispersion curves of C_4B_2 and C_4N_2 compounds, in both $AA'A''$ and ABC stacking configurations, are presented in figure 3. All spectra show 18 phonon branches, related to the 6 atoms present in the primitive cell. All those systems are dynamically stable since there are only positive frequencies.

Next, we computed the elastic constants of the systems using equation (1) to verify their mechanical stability, according to the Born stability criteria ($C_{11} > 0$ and $C_{12} < C_{11}$) [37]. Table II presents the elastic constants C_{11} , C_{12} , and $C_{44} = (C_{11} - C_{12})/2$, Young's modulus $Y^{2D} = (C_{11}^2 - C_{12}^2)/C_{11}$, and the Poisson ratio $\nu = C_{12}/C_{11}$ of C_4X_2 trilayers ($X = B$ or N), as well as those of several other 2D materials for comparison. Accordingly, the C_4X_2 structures are mechanically stable since they satisfy the Born criteria, agreeing with the phonon dispersion spectra shown in figure 3. The C_4X_2 nanosheets present high Young's modulus values and characteristics of isotropic systems since their Pois-

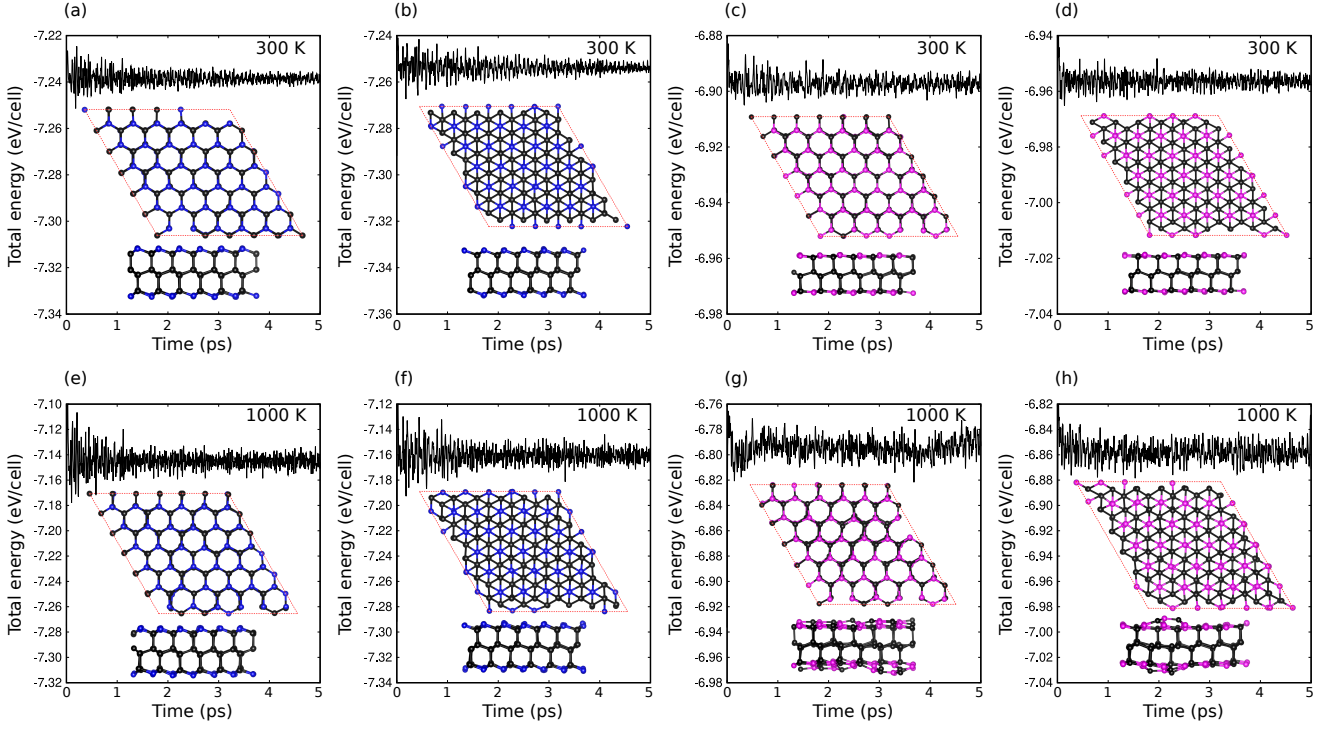


FIG. 2. Systems' total energy variation during 5 ps, computed with AIMD simulations. At 300 K, results of (a) AA'A''-C₄N₂, (b) ABC-C₄N₂, (c) AA'A''-C₄B₂, and (d) ABC-C₄B₂. At 1000 K, results of (e) AA'A''-C₄N₂, (f) ABC-C₄N₂, (g) AA'A''-C₄B₂, and (h) ABC-C₄B₂.

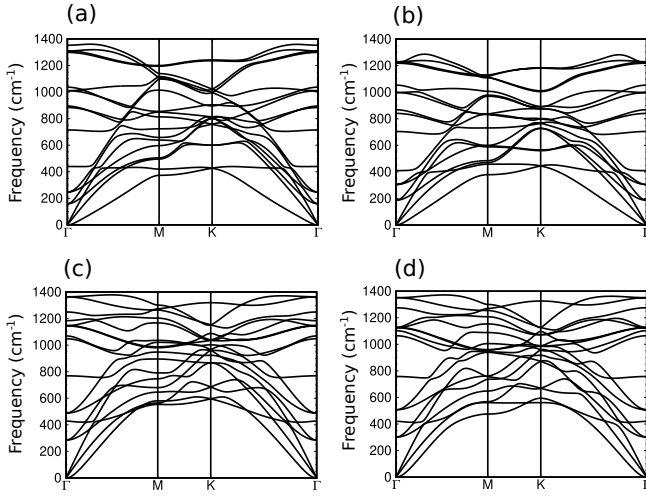


FIG. 3. Phonon dispersion branches of (a) AA'A''-C₄B₂, (b) ABC-C₄B₂, (c) AA'A''-C₄N₂, and (d) ABC-C₄N₂ along the main high-symmetry directions in the BZ of the hexagonal lattice.

son ratio σ values are lower than 0.5 [40, 41].

TABLE II. Elastic constants C_{11} , C_{12} , and C_{44} , Young's modulus Y^{2D} , Poisson ratio σ , formal density ρ_{2D} , longitudinal v_{LA} and transverse v_{TA} acoustic velocities of C₄X₂ (X = B or N), graphene, and other 2D diamonds. Elastic constants and Young's modulus are given in N/m, Poisson ratio is dimensionless, formal density and velocities are given in 10⁻⁷ kg/m² and km/s, respectively. The results with the * symbols were obtained using the data from the table and the equations described in this paper.

System	C_{11}	C_{12}	C_{44}	Y^{2D}	σ	ρ_{2D}	v_{LA}	v_{TA}
AA'A''-C ₄ N ₂	816	85	366	808	0.10	24.8	18.1	12.1
ABC-C ₄ N ₂	777	82	348	769	0.11	24.5	17.8	11.9
AA'A''-C ₄ B ₂	627	88	270	615	0.14	18.9	18.2	11.9
ABC-C ₄ B ₂	609	92	259	595	0.15	18.7	18.0	11.7
Graphene	354 ^a	60 ^a	147 [*]	340 ^b	0.18 ^c	7.55 ^c	21.6 [*]	13.9 [*]
HD	474 ^c	36 ^c	219 [*]	471 [*]	0.08 ^c	14.9 ^c	17.8 ^c	12.2 ^c
ABC-HD	718 ^c	58 ^c	330	713 [*]	0.08 ^c	22.2 ^c	18.0 ^c	12.2 ^c
FD	485 ^d	49 [*]	218 [*]	480 ^d	0.10 [*]		14.0 ^e	9.3 ^e
NCCN	568 ^f	66 ^f	243 ^f	560 [*]	0.12 [*]			
Diamond	1079 ^f	124 ^f	578 ^f				18.3 ^c	12.4 ^c

^a Reference [28]

^b Reference [38] - experiments

^c Reference [39]

^d Reference [15]

^e Reference [4]

^f Reference [9]

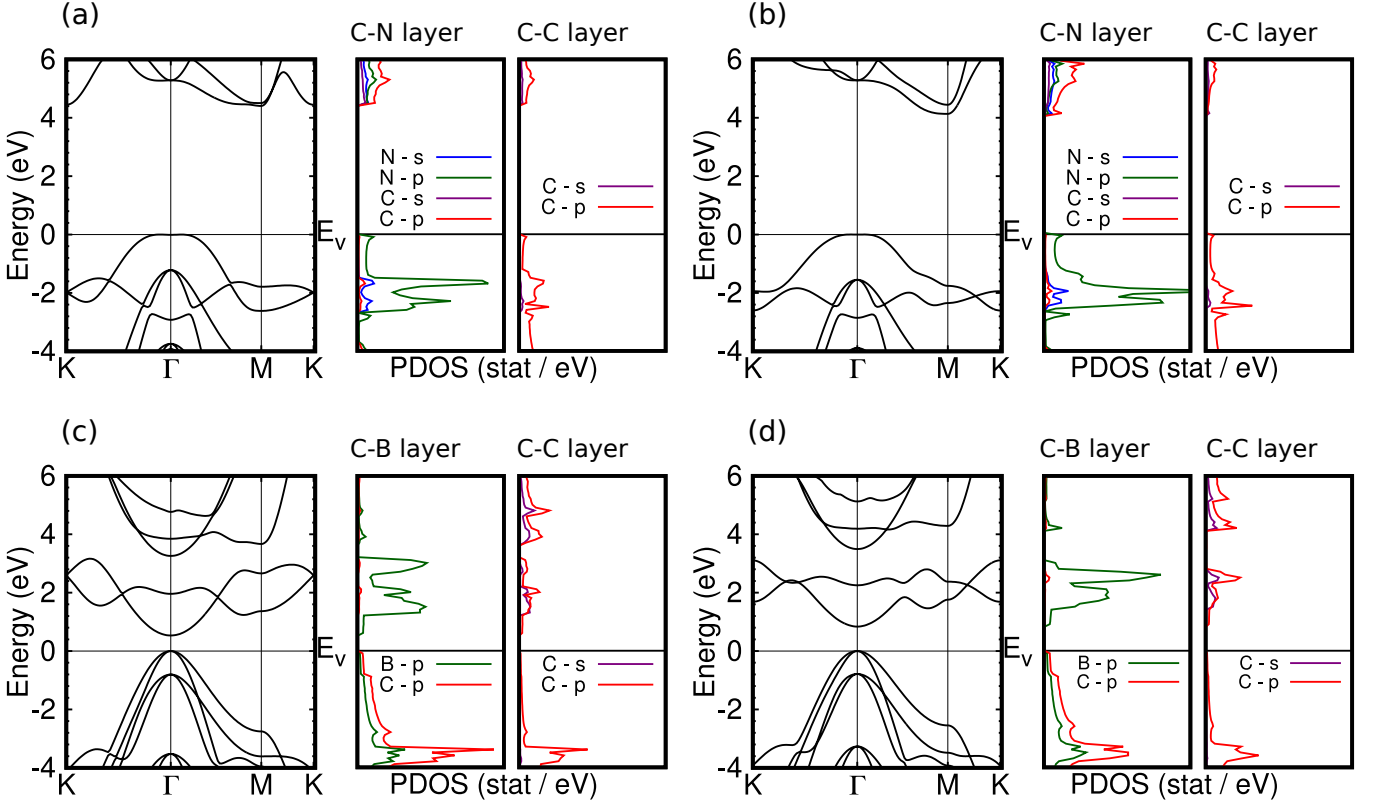


FIG. 4. Electronic band structures along the main high-symmetry directions of the BZ and PDOS, obtained with the optB88-vdW approach for the exchange-correlation energy: (a) AA'A''-C₄N₂, (b) ABC-C₄N₂, (c) AA'A''-C₄B₂, and (d) ABC-C₄B₂. The PDOS on the C and X *s*-orbitals are given in purple and blue, respectively, and on the C and X *p*-orbitals are given in red and green, respectively. E_v represents the VBM. Energies and PDPS are given in eV and states/eV, respectively.

Additionally, we estimated the longitudinal and the transversal acoustic velocities, given respectively by

$$v_{\text{LA}} = \left(\frac{C_{11}}{\rho_{2\text{D}}} \right)^{1/2} \quad \text{and} \quad v_{\text{TA}} = \left(\frac{C_{44}}{2\rho_{2\text{D}}} \right)^{1/2}, \quad (3)$$

where $\rho_{2\text{D}}$ is the formal density, allowing comparison among systems, independent of their thickness [4]. The velocity values, listed in Table II, suggest that the stiffness of the C₄X₂ systems is comparable with that of the diamond.

Following, we studied the electronic band structures and the projected density of states (PDOS) of the C₄X₂ systems, displayed in figure 4 (a)-(d). The electronic band structures and PDOS of AA'A''-C₄N₂ and ABC-C₄N₂ nanosheets, presented in figures 4 (a) and (b), exhibit some differences, despite their analogous PDOS, showing that the N *p*-orbitals dominate at valence band maximum (VBM) while the conduction band minimum (CBM) are mostly characterized by a mixture of *s*- and *p*-orbitals of N and C atoms. Both systems present the VBM around the Γ -point with a Mexican-hat dispersion, in which the two peaks lie on the Γ -K and Γ -M lines. The height of the Mexican-hat band at Γ point is 0.01 and 0.001 eV for AA'A''-C₄N₂ and ABC-C₄N₂, respectively. However, the CBM of ABC-C₄N₂ is well defined at the

M-valley, while in AA'A''-C₄N₂ although the CBM is located at the M-valley, the energy of the K-point is very close to the M-point one. On the other hand, the AA'A''-C₄B₂ and ABC-C₄B₂ nanosheets have very similar band structures, as shown in figures 4 (c) and (d). Both systems present direct band gaps, where the doubly degenerated VBM and the CBM are located at the Γ -point, in which the B *p*-orbitals dominate at the CBM and the VBM is described by a combination of B *p*-orbitals and C *p*-orbitals.

As discussed in the introduction, the 2D diamond systems present non-zero band gaps with characteristics that depend on several factors, such as doping with different functional groups. Herein, we are working with B and N atoms as X-doping elements, which the B atom belongs to group-III elements of the periodic table, with a $2s^22p^1$ valence electronic configuration, and the N atom belongs to group-V elements, with a $2s^22p^3$ valence electronic configuration. As a result, we found a wider indirect band gap for the C₄N₂ nanosheets, and a narrower direct band gap for the C₄B₂ systems when compared to PD. Table III displays the band gap values of the C₄X₂ nanosheets obtained with the optB88-vdW [22] (E_g^{vdW}) and the hybrid HSE [23] (E_g^{HSE}) functional approaches for the exchange-correlation energy. For com-

TABLE III. Electronic band gap values of C_4X_2 ($X = B$ or N) nanosheets (in eV), obtained with two different approximations for the exchange-correlation functional: optB88-vdW (E_g^{vdW}) [22] and HSE (E_g^{HSE}) [23]. The PD band gap value is also displayed. The electron (m_e^*) and hole (m_h^*) effective masses, in m_0 units, obtained with the optB88-vdW approach are also shown. The VBM of C_4B_2 systems are doubly degenerated at Γ and have two values for hole carrier. The CBM of C_4N_2 systems displays two effective masses around the M-valley, $m_e^{*M \rightarrow \Gamma}$ and $m_e^{*M \rightarrow K}$.

System	E_g^{vdW}	E_g^{PBE}	E_g^{HSE}	Band gap	m_h^*	m_e^*	$m_e^{*M \rightarrow \Gamma}$	$m_e^{*M \rightarrow K}$
AA'A''-C ₄ N ₂	4.40		5.56	indirect	6.23		2.94	0.30
ABC-C ₄ N ₂	4.13		5.42	indirect	16.77		2.61	0.47
AA'A''-C ₄ B ₂	0.53		1.64	direct	0.34 (0.68)	1.22		
ABC-C ₄ B ₂	0.84		1.97	direct	0.36 (0.80)	1.30		
HD ^a		3.32		direct	0.21 (0.58)	1.11		
FD ^a		4.04		direct	0.37 (1.13)	0.55		
PD ^b			2.70	indirect				

^a Reference [15]

^b Reference [8]. The ($\bar{2}110$)-oriented h-diamane with 3 graphene layers.

parison, we also included the HD and FD band gap values acquired with PBE functional [15] and of the three-layer graphene PD obtained with hybrid HSE functional [8]. The band gap width of the latter is 2.70 eV, while for the AA'A''-C₄N₂, ABC-C₄N₂, AA'A''-C₄B₂, and ABC-C₄B₂ functionalized compounds they are 5.56, 5.42, 1.64 eV, and 1.97 eV, respectively, using the same exchange-correlation functional. The C₄N₂ nanosheets have band gap width values, obtained with the optB88-vdW approach, similar to those of the HD and FD systems obtained with the PBE approximation.

Furthermore, since effective masses (m^*) can be used to investigate electronic transport under the influence of electric fields or carrier gradients, we estimated them by fitting parabolic functions to the CBM and VBM via the formula as follows:

$$\frac{1}{m^*} = \frac{1}{\hbar^2} \left| \frac{\partial^2 E(k)}{\partial k^2} \right| \quad (4)$$

where $E(k)$ and k are the energy and the wave vector of the CBM or VBM. The values of the effective masses depend on the curvature radius of the electronic band around the band-edge position, i.e., a larger curvature radius implies a heavier effective mass.

The electron (m_e^*) and hole (m_h^*) effective masses, in m_0 units, calculated with the optB88-vdW approach, are presented in table III. In both stacking structures of the C₄B₂ nanosheets, the effective masses of electrons and holes are comparable to the ones of HD and FD systems, which present extraordinary carriers mobility [15]. Furthermore, these estimated effective masses are similar to the $m_e^* = 1.06 m_0$ and $m_h^* = 0.59 m_0$ of silicon at a temperature of 4K [42]. Regarding C₄N₂ nanosheets, the m_h^* is the magnitude of the effective mass at Γ -point, i.e., we fitted a parabolic function considering the minimum located at the Γ -point [43]. Accordingly, the m_h^* depends on the height of the Mexican-hat band and the radius

centered at Γ -point around band edges [43]. On the other hand, the m_e^* displays two effective masses around the M-valley. $m_e^{*M \rightarrow \Gamma}$ shows a high electron effective mass, much higher than $m_e^{*M \rightarrow K}$. $m_e^{*M \rightarrow \Gamma}$ is five times larger than $m_e^{*M \rightarrow K}$ for ABC-C₄N₂ and nine times larger for AA'A''-C₄N₂.

Considering the stable structures presented previously and their physical properties, it is interesting to explore their potential applications. Further investigations could explore the applicability of C₄N₂ and C₄B₂ structures as building blocks to build 2D/3D systems, such as van der Waals heterostructures, with different properties [10, 44, 45]. Moreover, wide band gap materials, such as hexagonal boron nitride (h-BN), serve as a substrate for high-mobility 2D devices [46], a host material for single-photon emitter defect-centers for quantum computing and biosensors [4], etc. Therefore, the C₄N₂ nanosheets seem appropriate for these kinds of applications. Finally, the C₄B₂ nanosheets presented direct band gaps, in the 1.6 - 2.0 eV range, being more favorable for optoelectronics applications than C₄N₂ ones, which have indirect band gaps in the 5.4 - 5.6 eV range [46]. In particular, the small effective masses and high elastic modulus of C₄B₂ systems may contribute to high electron mobility [15], being suitable to be applied in photovoltaic cells. Table IV summarizes their properties and the respective potential applications.

In conclusion, we performed an *ab-initio* investigation on the structural, thermodynamic, dynamic, elastic, and electronic properties of C₄X₂ ($X = B$ or N) systems. According to AIMD simulations, phonon calculations, and the Born stability criteria, all the nanosheets are thermodynamically, dynamically, and mechanically stable. Furthermore, the systems presented standard enthalpy of formation close to the recently synthesized pristine 2D diamond composed of three graphene layers. Elastic properties indicated that those nanosheets possess a high Young's modulus values and characteristics of isotropic

TABLE IV. Summary of the qualitative properties and potential applications of C_4X_2 ($X = B$ or N) systems. The column indicates dynamic (DS), mechanic (MS), and thermodynamic (TS) stability, Young's modulus Y^{2D} , and effective masses (m^*).

System	DS	MS	TS (300 K)	TS (1000 K)	Y^{2D}	Stiffness	Band gap	m^*	Potential applications
C_4N_2	Yes	Yes	Yes	Yes	high	high	indirect	heavier	host material for single photon emission quantum computing/biosensors
C_4B_2	Yes	Yes	Yes	No	high	high	direct	lighter	nano-optics/nanoelectronics

systems, and the estimated longitudinal and transversal acoustic velocities revealed that their stiffness is comparable with that of the diamond. Finally, the systems' electronic properties presented some differences, in which C_4N_2 structures exhibited wide indirect band gaps and heavier effective masses, while the C_4B_2 ones had narrow direct band gaps and lighter effective masses. These results provide chemical routes to tune the electronic properties of 2D diamonds by doping them for specific applications, such as optoelectronic devices.

ACKNOWLEDGMENTS

Brazilian Federal Government Agencies CAPES (Grants 88882.332907/2019-01 and 88887.371193/2019-

00), CNPq (Grants 314884/2021-1, 302800/2022-0, and 150595/2023-9) and FAPESP (Grant 22/10095-8) partially supported this investigation. The authors acknowledge the National Laboratory for Scientific Computing (LNCC/MCTI, Brazil) for providing HPC resources of the Santos Dumont supercomputer, Centro Nacional de Processamento de Alto Desempenho em São Paulo (CENAPAD-SP, Brazil) and SNIC-UPPMAX, SNIC-HPC2N, and SNIC-NSC centers under the Swedish National Infrastructure for Computing (SNIC) resources.

-
- [1] K. S. Novoselov, A. K. Geim, S. V. Morozov, D. Jiang, Y. Zhang, S. V. Dubonos, I. V. Grigorieva, and A. A. Firsov, Electric field effect in atomically thin carbon films, *Science* **306**, 666 (2004).
- [2] A. K. Geim and K. S. Novoselov, The rise of graphene, *Nature Materials* **6**, 183 (2007).
- [3] Y. Gao, T. Cao, F. Cellini, C. Berger, W. A. De Heer, E. Tosatti, E. Riedo, and A. Bongiorno, Ultrahard carbon film from epitaxial two-layer graphene, *Nature Nanotechnology* **13**, 133 (2018).
- [4] P. B. Sorokin and B. I. Yakobson, Two-dimensional diamond—diamane: current state and further prospects, *Nano Letters* **21**, 5475 (2021).
- [5] G. Qin, L. Wu, and H. Gou, Diamane: design, synthesis, properties, and challenges, *Functional Diamond* **1**, 83 (2021).
- [6] F. Piazza, K. Gough, M. Monthieux, P. Puech, I. Gerber, R. Wiens, G. Paredes, and C. Ozoria, Low temperature, pressureless sp^2 to sp^3 transformation of ultrathin, crystalline carbon films, *Carbon* **145**, 10 (2019).
- [7] E. D. Grayfer, V. G. Makotchenko, L. S. Kibis, A. I. Boronin, E. M. Pazhetnov, V. I. Zaikovskii, and V. E. Fedorov, Synthesis, properties, and dispersion of few-layer graphene fluoride, *Chemistry—An Asian Journal* **8**, 2015 (2013).
- [8] F. Ke, L. Zhang, Y. Chen, K. Yin, C. Wang, Y.-K. Tzeng, Y. Lin, H. Dong, Z. Liu, J. S. Tse, *et al.*, Synthesis of atomically thin hexagonal diamond with compression, *Nano Letters* **20**, 5916 (2020).
- [9] T. Pakornchote, A. Ektarawong, W. Busayaporn, U. Pinsook, and T. Bovornratanaraks, Roles of nitrogen substitution and surface reconstruction in stabilizing non-passivated single-layer diamond, *Physical Review B* **102**, 075418 (2020).
- [10] B. Ipaves, J. F. Justo, and L. V. C. Assali, Carbon-related bilayers: Nanoscale building blocks for self-assembly nanomanufacturing, *The Journal of Physical Chemistry C* **123**, 23195 (2019).
- [11] C. He, M. Zhang, T. Li, and W. Zhang, Electric field-modulated high sensitivity and selectivity for nh_3 on α - c_2n_2 nanosheet: Insights from dft calculations, *Applied Surface Science* **505**, 144619 (2020).
- [12] L. Tan, C. Nie, Z. Ao, H. Sun, T. An, and S. Wang, Novel two-dimensional crystalline carbon nitrides beyond gc_3n_4 : structure and applications, *Journal of Materials Chemistry A* **9**, 17 (2021).
- [13] L. Zhu and T. Zhang, Suppressed thermal conductivity in fluorinated diamane: optical phonon dominant thermal transport, *Applied Physics Letters* **115**, 151904 (2019).
- [14] F. Cellini, F. Lavini, T. Cao, W. de Heer, C. Berger, A. Bongiorno, and E. Riedo, Epitaxial two-layer graphene under pressure: diamene stiffer than diamond, *FlatChem* **10**, 8 (2018).
- [15] T. Cheng, Z. Liu, and Z. Liu, High elastic moduli, controllable bandgap and extraordinary carrier mobility in single-layer diamond, *Journal of Materials Chemistry C* **8**, 13819 (2020).
- [16] W. Kohn and L. J. Sham, Self-consistent equations in-

- cluding exchange and correlation effects, *Physical Review* **140**, A1133 (1965).
- [17] G. Kresse and D. Joubert, From ultrasoft pseudopotentials to the projector augmented-wave method, *Physical Review B* **59**, 1758 (1999).
- [18] P. Giannozzi, S. Baroni, N. Bonini, M. Calandra, R. Car, C. Cavazzoni, D. Ceresoli, G. L. Chiarotti, M. Cococcioni, I. Dabo, *et al.*, Quantum espresso: a modular and open-source software project for quantum simulations of materials, *Journal of Physics: Condensed Matter* **21**, 395502 (2009).
- [19] P. Giannozzi, O. Andreussi, T. Brumme, O. Bunau, M. B. Nardelli, M. Calandra, R. Car, C. Cavazzoni, D. Ceresoli, and M. *et al.* Cococcioni, Advanced capabilities for materials modelling with quantum espresso, *Journal of Physics: Condensed Matter* **29**, 465901 (2017).
- [20] J. P. Perdew, K. Burke, and M. Ernzerhof, Generalized gradient approximation made simple, *Physical Review Letters* **77**, 3865 (1996).
- [21] M. Dion, H. Rydberg, E. Schröder, D. C. Langreth, and B. I. Lundqvist, Van der waals density functional for general geometries, *Physical Review Letters* **92**, 246401 (2004).
- [22] J. Klimeš, D. R. Bowler, and A. Michaelides, Chemical accuracy for the van der waals density functional, *Journal of Physics: Condensed Matter* **22**, 022201 (2009).
- [23] J. Heyd, G. E. Scuseria, and M. Ernzerhof, Hybrid functionals based on a screened coulomb potential, *The Journal of Chemical Physics* **118**, 8207 (2003).
- [24] H. J. Monkhorst and J. D. Pack, Special points for brillouin-zone integrations, *Physical Review B* **13**, 5188 (1976).
- [25] S. Baroni, S. De Gironcoli, A. Dal Corso, and P. Giannozzi, Phonons and related crystal properties from density-functional perturbation theory, *Reviews of Modern Physics* **73**, 515 (2001).
- [26] J. C. Garcia, D. B. de Lima, L. V. C. Assali, and J. F. Justo, Group IV graphene- and graphane-like nanosheets, *The Journal of Physical Chemistry C* **115**, 13242 (2011).
- [27] B. Ipaves, J. F. Justo, and L. V. Assali, Aluminum functionalized few-layer silicene as anode material for alkali metal ion batteries, *Molecular Systems Design & Engineering* **8**, 379 (2023).
- [28] E. Cadelano, P. L. Palla, S. Giordano, and L. Colombo, Elastic properties of hydrogenated graphene, *Physical Review B* **82**, 235414 (2010).
- [29] B. Ipaves, J. F. Justo, and L. V. C. Assali, Functionalized few-layer silicene nanosheets: stability, elastic, structural, and electronic properties, *Physical Chemistry Chemical Physics* **24**, 8705 (2022).
- [30] R. Larico, L. V. C. Assali, W. V. M. Machado, and J. F. Justo, Isolated nickel impurities in diamond: A microscopic model for the electrically active centers, *Applied Physics Letters* **84**, 720 (2004).
- [31] L. V. C. Assali, W. V. M. Machado, and J. F. Justo, Manganese impurities in boron nitride, *Applied Physics Letters* **89**, 072102 (2006).
- [32] L. V. C. Assali, W. V. M. Machado, and J. F. Justo, 3d transition metal impurities in diamond: electronic properties and chemical trends, *Physical Review B* **84**, 155205 (2011).
- [33] S. Hastrup, M. Strange, M. Pandey, T. Deilmann, P. S. Schmidt, N. F. Hinsche, M. N. Gjerding, D. Torelli, P. M. Larsen, A. C. Riis-Jensen, and *et al.*, The computational 2d materials database: high-throughput modeling and discovery of atomically thin crystals, *2D Materials* **5**, 042002 (2018).
- [34] M. L. Marcondes, S. S. M. Santos, I. P. Miranda, P. Rocha-Rodrigues, L. V. C. Assali, A. M. L. Lopes, J. P. Araújo, and H. M. Petrilli, On the stability of calcium and cadmium based ruddlesden–popper and double perovskite structures, *The Journal of Materials Chemistry C* **9**, 15074 (2021).
- [35] G. Kresse and J. Furthmüller, Efficient iterative schemes for ab initio total-energy calculations using a plane-wave basis set, *Physical Review B* **54**, 11169 (1996).
- [36] T. Pakornchote, A. Ektarawong, B. Alling, U. Pinsook, S. Tancharakorn, W. Busayaporn, and T. Bovornratnaraks, Phase stabilities and vibrational analysis of hydrogenated diamondized bilayer graphenes: A first principles investigation, *Carbon* **146**, 468 (2019).
- [37] F. Mouhat and F.-X. Coudert, Necessary and sufficient elastic stability conditions in various crystal systems, *Physical Review B* **90**, 224104 (2014).
- [38] C. Lee, X. Wei, J. W. Kysar, and J. Hone, Measurement of the elastic properties and intrinsic strength of monolayer graphene, *Science* **321**, 385 (2008).
- [39] L. A. Chernozatonskii, P. B. Sorokin, A. A. Kuzubov, B. P. Sorokin, A. G. Kvashnin, D. G. Kvashnin, P. V. Avramov, and B. I. Yakobson, Influence of size effect on the electronic and elastic properties of diamond films with nanometer thickness, *The Journal of Physical Chemistry C* **115**, 132 (2011).
- [40] H. Gercek, Poisson’s ratio values for rocks, *International Journal of Rock Mechanics and Mining Sciences* **44**, 1 (2007).
- [41] P. Hess, Bonding, structure, and mechanical stability of 2d materials: the predictive power of the periodic table, *Nanoscale Horizons* **6**, 856 (2021).
- [42] M. A. Green, Intrinsic concentration, effective densities of states, and effective mass in silicon, *Journal of Applied Physics* **67**, 2944 (1990).
- [43] D. Wickramaratne, F. Zahid, and R. K. Lake, Electronic and thermoelectric properties of van der waals materials with ring-shaped valence bands, *Journal of Applied Physics* **118**, 075101 (2015).
- [44] K. S. Novoselov, A. Mishchenko, A. Carvalho, and A. H. Castro Neto, 2d materials and van der waals heterostructures, *Science* **353**, aac9439 (2016).
- [45] J. C. Garcia, J. F. Justo, W. V. M. Machado, and L. V. C. Assali, Functionalized adamantane: building blocks for nanostructure self-assembly, *Physical Review B* **80**, 125421 (2009).
- [46] A. Chaves, J. G. Azadani, H. Alsalman, D. Da Costa, R. Frisenda, A. Chaves, S. H. Song, Y. D. Kim, D. He, J. Zhou, *et al.*, Bandgap engineering of two-dimensional semiconductor materials, *npj 2D Materials and Applications* **4**, 29 (2020).